Journal of the Meteorological Society of Japan, Vol. 72, No. 4, pp. 569–587, 1994

Chaotic Lagrangian Motion and Heat Transport in a Steady, Baroclinic Annulus Wave

By Seiji Sugata

The National Institute for Environmental Studies, Tsukuba, Ibaraki 305, Japan

and

Shigeo Yoden

Department of Geophysics, Kyoto University, Kyoto 606-01, Japan

(Manuscript received 21 October 1993, in revised form 9 May 1994)

Abstract

Lagrangian motion in a steady, baroclinic annulus wave is investigated numerically by following a tracer particle trajectory for a long period. Even for the regular Eulerian flow field of steady waves, the trajectory shows a chaotic nature, which is an example of "Lagrangian turbulence". However, the chaotic trajectory has some organized structures depending on its position in the annulus. Based on the structure, the annulus of fluid is divided into the following regions: the upper-level and lower-level jets, the cyclonically and anticyclonically trapped regions, and the inner, outer and lower boundary layers. Some isolated regions in which the marked particle has never stayed for that period are also found inside the cyclonically trapped region and around the anticyclonically trapped region. Statistics over the long period show a preferred cyclic route of the region transitions: the outer boundary layer → the upper-level jet → the inner boundary layer → the lower-level jet or the lower boundary layer → the outer boundary layer. The number of dwell periods of the particle in the trapped regions is much smaller than that in the cyclic route, but the average time of one stay in the trapped regions is longer.

A Lagrangian view of the heat transport in the steady annulus wave is obtained: The fluid particle absorbs a large amount of heat in the outer boundary layer and releases it in the inner boundary layer, while it nearly conserves its temperature in the interior regions. Inward heat transport is small in every one cycle of the meander of the jets.

1. Introduction

Lagrangian motion of fluid particles and fluid elements has been studied for several decades in the field of dynamic meteorology and physical oceanography. A good historical review is given by Pierrehumbert (1991a). Earliest examples of such studies are papers by Rossby *et al.* (1937) and Welander (1955), in which deformation and mixing of a fluid element were discussed with aerological data and experimental results, respectively. Both of the papers treat basic and important properties of the Lagrangian motion and are still worth referring to.

Trajectories of the Lagrangian motion might be very complicated even if the Eulerian flow field is regular and coherent. Flierl (1981) investigated particle motions in some idealized two-dimensional flow fields of steadily propagating waves and isolated circular eddies, aiming at a possible application to Lagrangian data of the trajectories of surface drifters in the ocean. He showed that some particles are trapped to translate along with the disturbances when a particle speed is comparable to or larger than the phase speed, c. Introduction of the "co-moving" reference frame with the wave or the isolated eddy, $(X, Y) = (x - ct,\ y)$, was very effective to analyze the drift rates and trapped areas; the trajectories in this frame are given by

$$\left\{ \begin{array}{rcl} \dot{X} & = & -\dfrac{\partial}{\partial Y}\Psi(X,Y), \\ \dot{Y} & = & \dfrac{\partial}{\partial X}\Psi(X,Y). \end{array} \right. \tag{1}$$

If a streamline $\Psi(X, Y) = \Psi_1$ is a closed orbit, particles on it are trapped with the disturbance. The largest orbit separating regions of trapped and untrapped particles is a heteroclinic orbit connecting

---

Fig. 1. A streak photograph of trajectories of the suspended particles at a depth of 0.5 cm below the upper surface by exposing the film for 2 seconds in a camera mounted on the rotating apparatus, taken from Hide and Mason (1975). Working fluid is a water-glycerol solution. The size of the annulus is $b - a = 4.64$ cm and $d = 13.5$ cm. Rotation rate is 3.22 rad/s and the thermal Rossby number is 0.118.

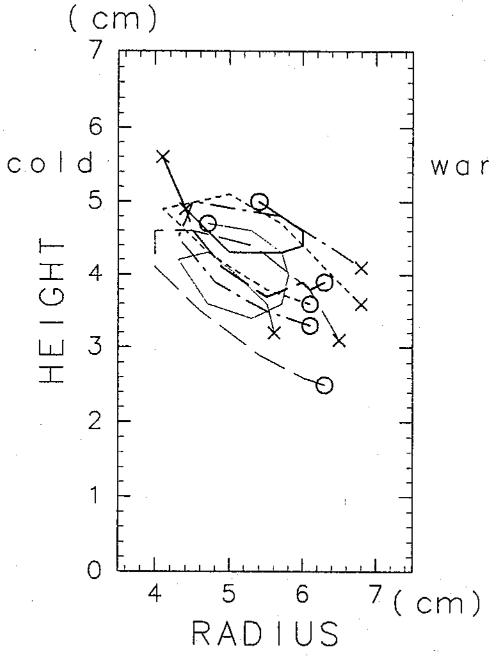

Fig. 2. Trajectories of particles projected onto the meridional plane, which were obtained by tracing the motion of suspended balls of acrylic resin in the rotating annulus experiment performed by Sakai (1990). Symbols o and × indicate initial and final positions of the tracing particles, respectively. The size of the annulus is $a = 3.5$ cm, $b = 7.5$ cm, and $d = 7$ cm.

a pair of saddle points (Knobloch and Weiss, 1987; Weiss and Knobloch, 1989).

If the propagating wave is modulated, that is, the streamfunction Ψ is time-periodic in Eq. (1), then the trajectories in the co-moving frame may be chaotic even though the Eulerian flow is laminar (Knobloch and Weiss, 1987; Weiss and Knobloch, 1989). "Chaotic advection" or "Lagrangian turbulence" (see *e.g.*, Ottino (1989) for fundamental descriptions) is really observed in a separatrix layer between the trapped and untrapped regions. Pierrehumbert (1991a, 1991b) investigated further the chaotic mixing by modulated propagating waves with computing finite-time Lyapunov exponents (see Yoden and Nomura, 1993) in physical space. The basic concept and analysis procedure of the chaotic mixing were applied to a rotating annulus experiment on Rossby waves by Behringer, Mayers and Swinney (1991) and to global GCM data by Pierrehumbert and Yang (1993).

If the flow field is three-dimensional, particle trajectories can be chaotic even for steady-state solutions, because the dynamical system describing the trajectories has three degrees of freedom:

$$\left\{\begin{array}{l} \dot{x} = u(x,y,z), \\ \dot{y} = v(x,y,z), \\ \dot{z} = w(x,y,z). \end{array}\right. \tag{2}$$

Simplest examples of such chaotic streamlines are the Arnold-Beltrami-Childress (ABC) flows (Dombre *et al.*, 1986) and the steady confined Stokes flows (Bajer and Moffatt, 1990).

Steady waves in the rotating annulus of fluid with radial differential heating are one of the familiar examples of such three-dimensional flows in the field of geophysical fluid dynamics. The Eulerian flow field of the steady waves has been investigated intensively by laboratory experiments (see a review by Hide and Mason, 1975) and by numerical experiments (*e.g.*, Williams, 1969, 1971, 1972; Ukaji and Tamaki, 1989). However, the Lagrangian motion in the steady waves has attracted little attention until now. Figure 1 shows a streak photograph of particle trajectories near the top surface of the fluid taken by a camera mounted on the rotating apparatus (Hide and Mason, 1975). Meandering of the "jet stream" is clearly visualized by long streaks. Particle trajectories in the interior region were obtained in the laboratory experiment by Sakai (1990). A projection of the trajectories on the meridional plane is

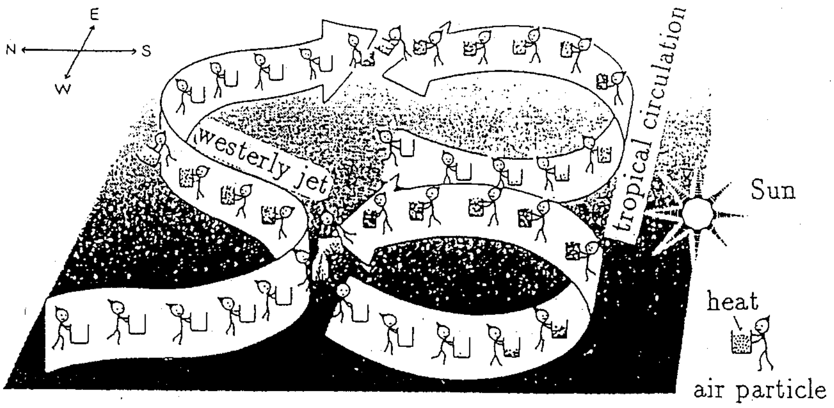

Fig. 3. A Lagrangian-type of illustration for the meridional heat transport in the atmosphere (Unno *et al.*, 1992).

nearly elliptic and the major axis tilts from upper inside (cold side) to lower outside (warm side) as shown in Fig 2. These figures show some aspects of the Lagrangian motion. However, it is difficult to get the chaotic nature of the trajectories from these figures because of the short exposure times and the limited number of particles.

Under the influence of recent progress in the study of Lagrangian turbulence, in this paper we investigate the Lagrangian motion of particles in a steady, baroclinic annulus wave by tracing the trajectories for a long time interval with a numerical solution obtained by Sugata and Yoden (1993). Even if the co-moving reference frame with the steadily propagating wave is adopted following Flierl (1981), the obtained trajectories are expected to be much more complicated than those in the ABC flows, because the Eulerian flow field we analyze is not a simple and ideal flow but a "real" one in the presence of rigid boundaries and viscosity. Therefore we take a new approach to get a gross feature of the chaotic nature of the particle trajectories; the annular domain is divided into several regions with different behavior of particles, and residence time in each region and transitions between the regions are computed.

The baroclinic annulus waves owe their existence to the radial differential heating, that is to say, the annulus waves have an important role in inward heat transport. The Eulerian mean description shows a positive correlation between inward deviatoric flow and positive deviatoric temperature in the interior region. Based on such results, illustrations of the heat transport from a Lagrangian viewpoint as shown in Fig. 3 are widely accepted for the meridional transport in the atmosphere. This figure was taken from a high-school textbook; air particles in the westerly jet stream obtain heat in low latitudes, move poleward, and release it in high latitudes. Heating and cooling of the particles take place in every cycle of the meander of the westerly jet. However, how well is this kind of illustration applicable to the Lagrangian view of the heat transport in the steady annulus waves?

In this paper, we straightforwardly compute the temperature change of the same particle used in the trajectory analysis. Moreover, a crude estimation of the heat transport from the Lagrangian view is done using the probability of transitions between the regions. It should be noted that temperature in the present study is conserved following the motion if thermal diffusion is absent, which condition is roughly fulfilled in the interior region. However, temperature is not a passive scalar because it is in the buoyancy term in the vertical momentum equation. Although enhanced transport is an interesting and important subject of the "Lagrangian turbulence", temperature is not the best physical quantity for that purpose. Chaotic mixing in the steady annulus waves is not investigated to any great extent in this study.

Lagrangian motion of particles in a steady annulus wave is investigated in Section 2 and a Lagrangian view of the heat transport is given in Section 3. Section 4 is for discussion and Section 5 for conclusions.

2. Chaotic particle motion in a steady wave solution

2.1 A steady wave solution

Sugata and Yoden (1993) developed a semi-spectral model which has the same experimental parameters as those used by Ukaji and Tamaki (1989). Discrepancy in the obtained steady waves is small between two models. Experimental parameters for the steady wave we investigate in this study are as follows. The dimensions of the apparatus are: inner radius a = 4.5 cm, outer radius b = 9.7 cm, and height of the fluid d = 8.0 cm. The top surface of the working fluid of water is in contact with a free-slip rigid lid and the other three surfaces are non-slip rigid boundaries. Inner and outer walls are kept at different temperatures to maintain the difference

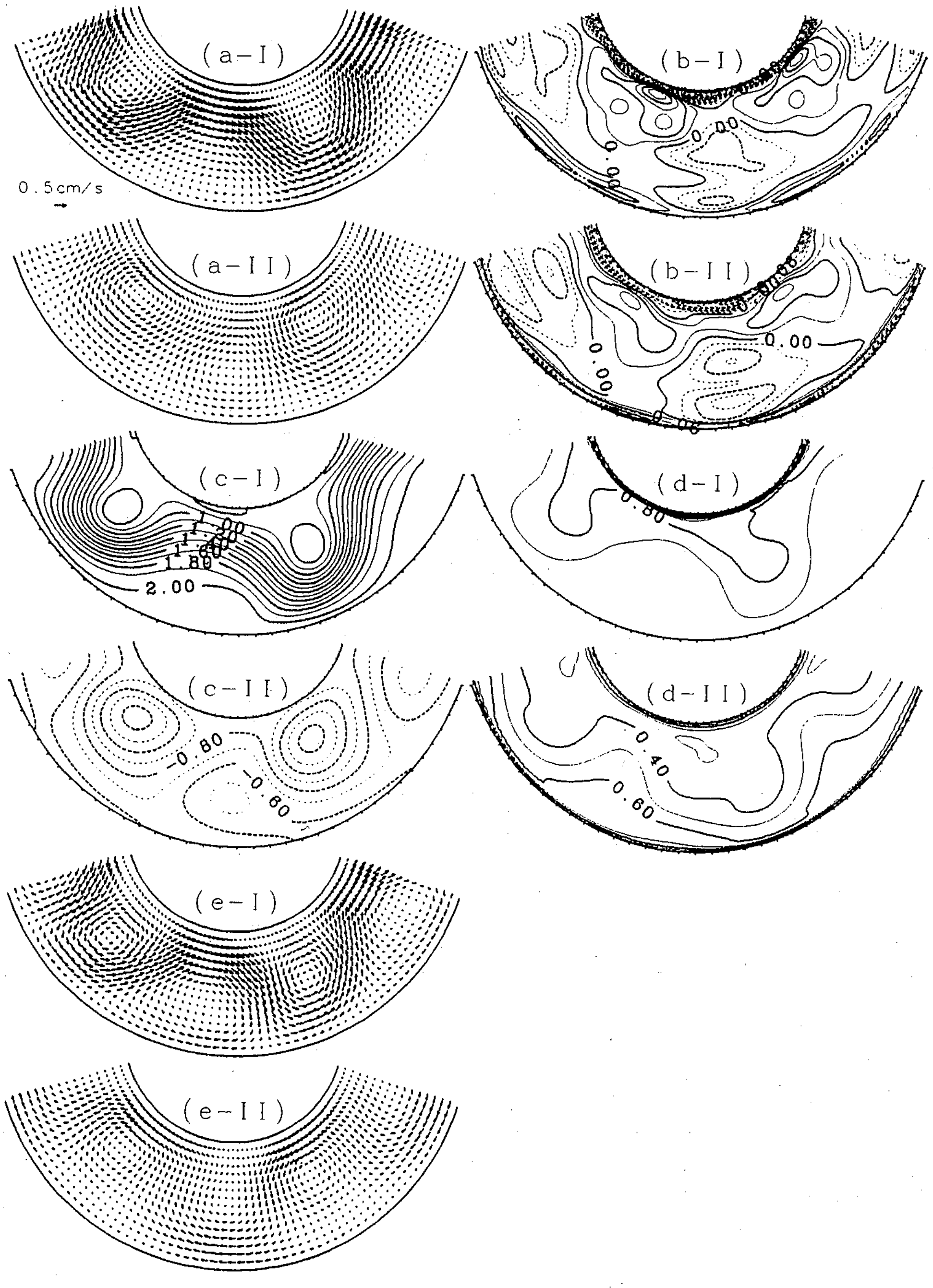

Fig. 4. Horizontal sections of a steady wave solution: (a) horizontal velocity field, (b) vertical velocity [cm/s], (c) pressure divided by mean density [$\mathrm{cm}^2/\mathrm{s}^2$], (d) normalized temperature, and (e) horizontal velocity field in the co-moving frame, at two different levels of $z/d = 3/4$ (I) and $1/4$ (II). Each section is described over two wavelengths in the azimuthal direction. Amplitudes of the unit vector and contour intervals are the same between sections for the same variable.

$\Delta T = 3$ K, and the top and bottom boundaries are thermally insulating. The rotation rate Ω of the apparatus is 0.6 rad/s. The thermal Rossby number (Ro_T) is 6.55×10^{-1} and the Taylor number (Ta) is 9.15×10^{6}. Refer to Sugata and Yoden (1993) for further description of the model and the numerical procedure.

The dominant wavenumber of the steady wave is $m = 5$. The wave drifts "eastward" relative to the apparatus at a constant rotation rate $\omega = 1.67 \times 10^{-2}$ rad/s. The term "east" means the azimuthal direction of the rotation of the apparatus. The rotation rate ω is about 1/36 of the apparatus rotation rate Ω.

Dependent variables computed in our model are velocity (u, v, w), normalized temperature θ, and

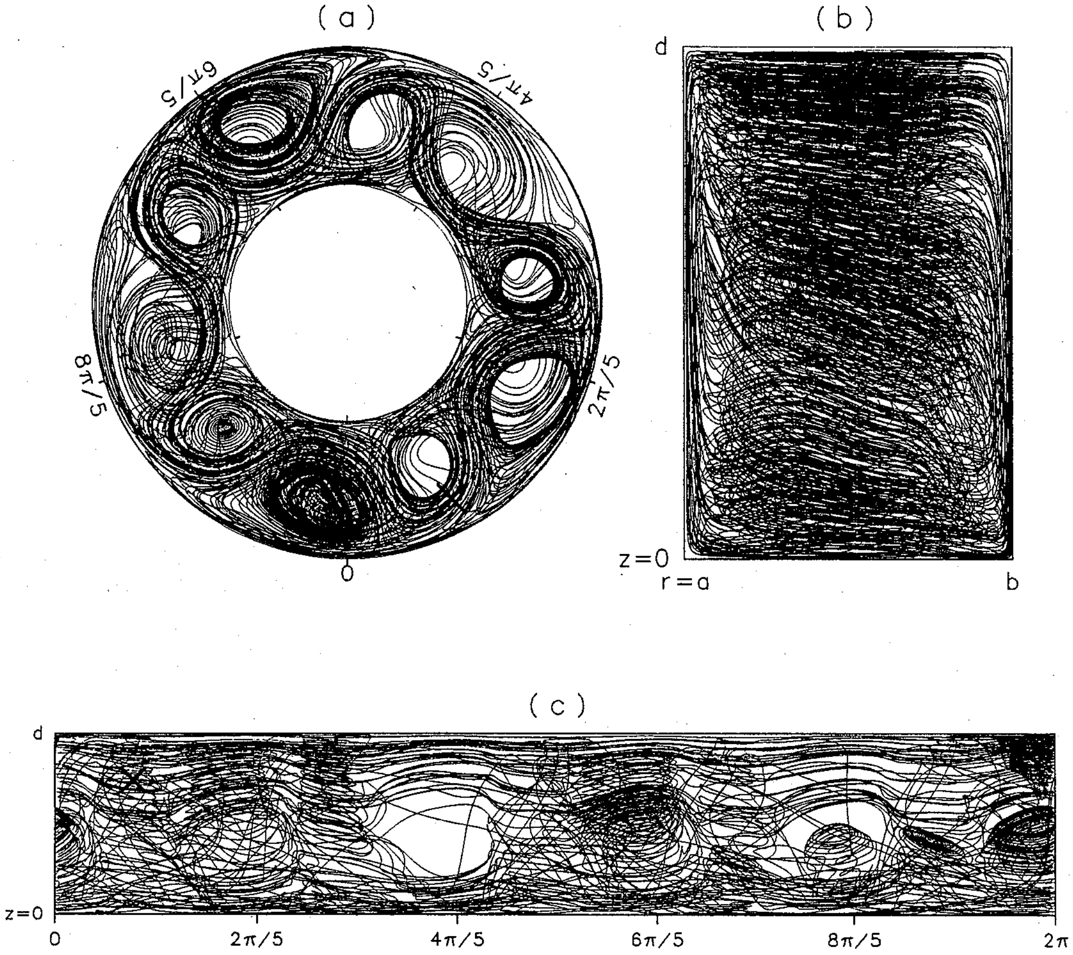

Fig. 5. Projections of a trajectory of a tracer particle onto r-λ' plane (a), r-z plane (b), and λ'-z plane (c), where λ' is the azimuth in the co-moving frame. The particle is initially located at a cross mark and traced for 5×10^4 s.

pressure divided by the mean density p. The velocity components (u, v, w) are related in the cylindrical coordinates (r, λ, z), as $(u, v, w) \equiv (\frac{Dr}{Dt}, r\frac{D\lambda}{Dt}, \frac{Dz}{Dt})$, where r, λ, and z are the radius from the axis of the rotation, the azimuth relative to the apparatus, and the height from the bottom, respectively, and D/Dt is the total derivative. Figure 4 shows (u, v), w, p, and θ, over two wavelengths at two different levels; an upper level of $z/d = 3/4$ (I) and a lower level of $z/d = 1/4$ (II). The three dimensional structure of the baroclinic annulus wave is basically the same as that obtained in early studies (Williams, 1969, 1971, 1972; Ukaji and Tamaki, 1989). A strong westerly jet stream is dominant at the upper level, as shown in Fig. 4(a-I). The horizontal velocity is over 0.5 cm/s at the core of the jet stream. At the lower level (a-II), the horizontal flow is weaker owing to the presence of the non-slip bottom boundary. The horizontal flow is almost parallel with isobars at both levels (c), which is indicative of the predominance of geostrophic balance. Downward motion is found in the western side of the low-pressure except for the inner boundary layer (b). Correlation between temperature (d) and the radial velocity (a) is indicative of inward heat transport by the baroclinic annulus wave.

Figure 4e shows the horizontal velocity (u, v') described in the co-moving frame in the azimuthal direction with $\lambda' = \lambda - \omega t$. The azimuthal velocity in this frame is given by $v' = r\frac{D\lambda'}{Dt} = v - r\omega$. Compared with Fig. 4a, the anticyclonic circulation in the high-pressure is clear at the upper level and an easterly jet stream appears clearly at the lower level, which feature are solely due to the addition of the apparent westward velocity, $-r\omega$ to v.

2.2 Numerical procedure of particle tracing

We consider an idealized tracer particle which is so small that it follows the flow faithfully and is so large that the stochastic process due to molecular motions is ignored. We also assume that the particle has the same physical properties as the experimental fluid, such as specific heat and den-

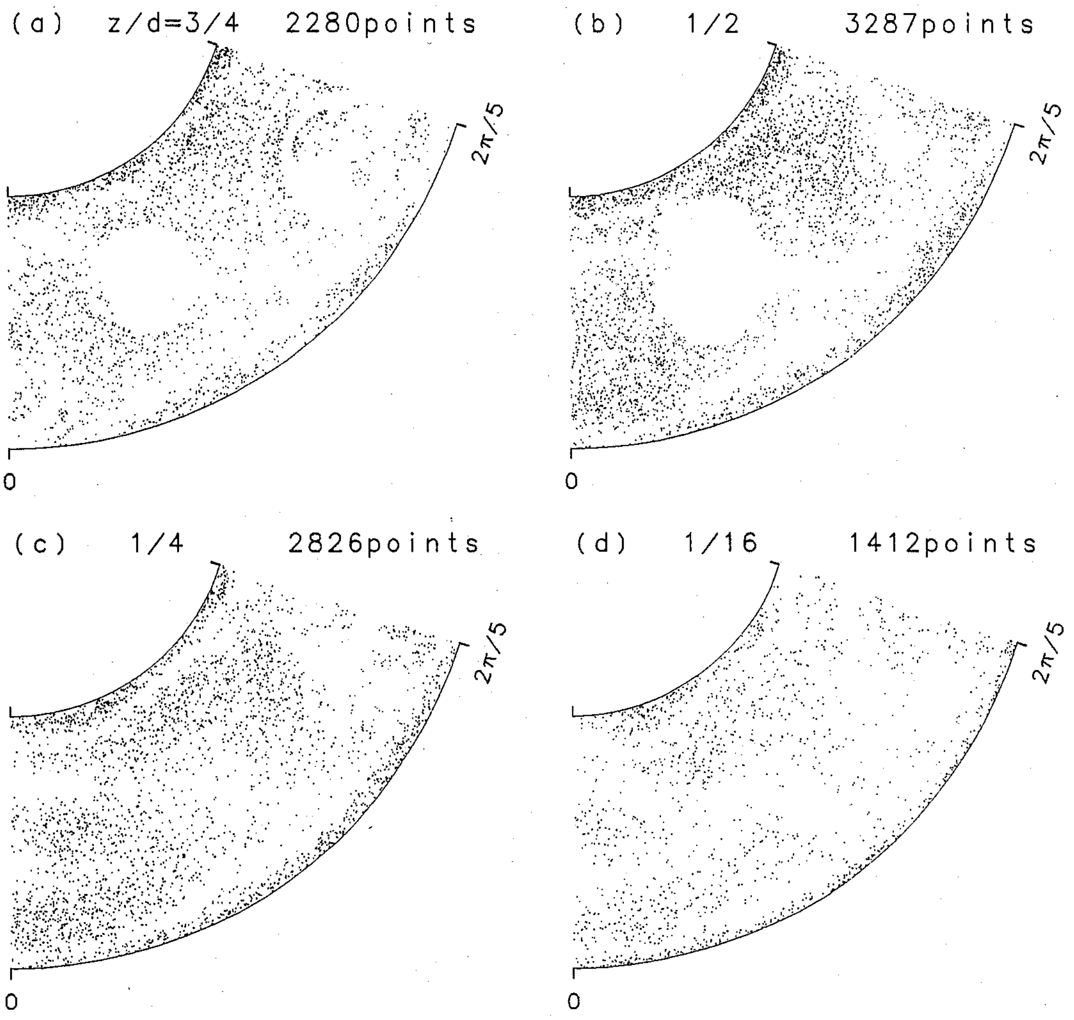

Fig. 6. Poincaré sections for a trajectory of 5×10^5 s period at four levels: $z/d = 3/4$ (a), 1/2 (b), 1/4 (c) and 1/16 (d). The $2\pi/5$ periodicity in λ' direction is used for the sections. The number of points is shown above each figure.

sity. The particle is released at a point $(r, \lambda, z) = (a + 3(b-a)/4, 7/18 \times 2\pi/5, 3d/4)$ in the core of the westerly jet stream, and is traced for 5×10^5 s with the velocity field described in the preceding subsection. It should be noted here that the obtained trajectory itself does not always keep its realism over the period owing to the chaotic nature of the system, an inevitable computational error, and the assumption on the tracer particle mentioned above. However, the long-period tracing of one particle would be justified because our main purpose is not exact prediction of the position of the marked particle but general description of the nature of the particle behavior. Present study based on the long-period tracing can be interpreted as an analysis of huge ensembles of "real" particle trajectories for a short-period with different initial positions. In other words, the long-period tracing is equivalent to a succession of the short-period tracings which are restarted from the final position of the previous tracing whilst clearing out the prediction error to zero.

Movement of the marked particle is obtained by integrating the kinematical relationship (2) between position and velocity of the particle, which is expressed in a centered difference form:

$$\boldsymbol{r}(t+\Delta t) = \boldsymbol{r}(t-\Delta t) + 2\boldsymbol{V}(\boldsymbol{r}(t), t)\Delta t, \tag{3}$$

where Δt is the time increment, which is set to 5.0×10^{-3} s, and $\boldsymbol{r}$ and $\boldsymbol{V}$ are three-dimensional vectors of position and velocity of the particle relative to the apparatus, respectively. To prevent the growth of a numerical mode, a periodical restart is done every 12.5 s.

A dependent variable $q(r, \lambda, z)$ is linearly interpolated from those of the adjacent four grids, $q_{i,j}, q_{i+1,j}, q_{i,j+1}, q_{i+1,j+1}$, in the meridional plane as follows.

$$\begin{aligned} q(r,\lambda,z) &= (1-x)(1-y)q_{i,j} + x(1-y)q_{i+1,j} \\ &\quad + (1-x)yq_{i,j+1} + xyq_{i+1,j+1}. \end{aligned} \tag{4}$$

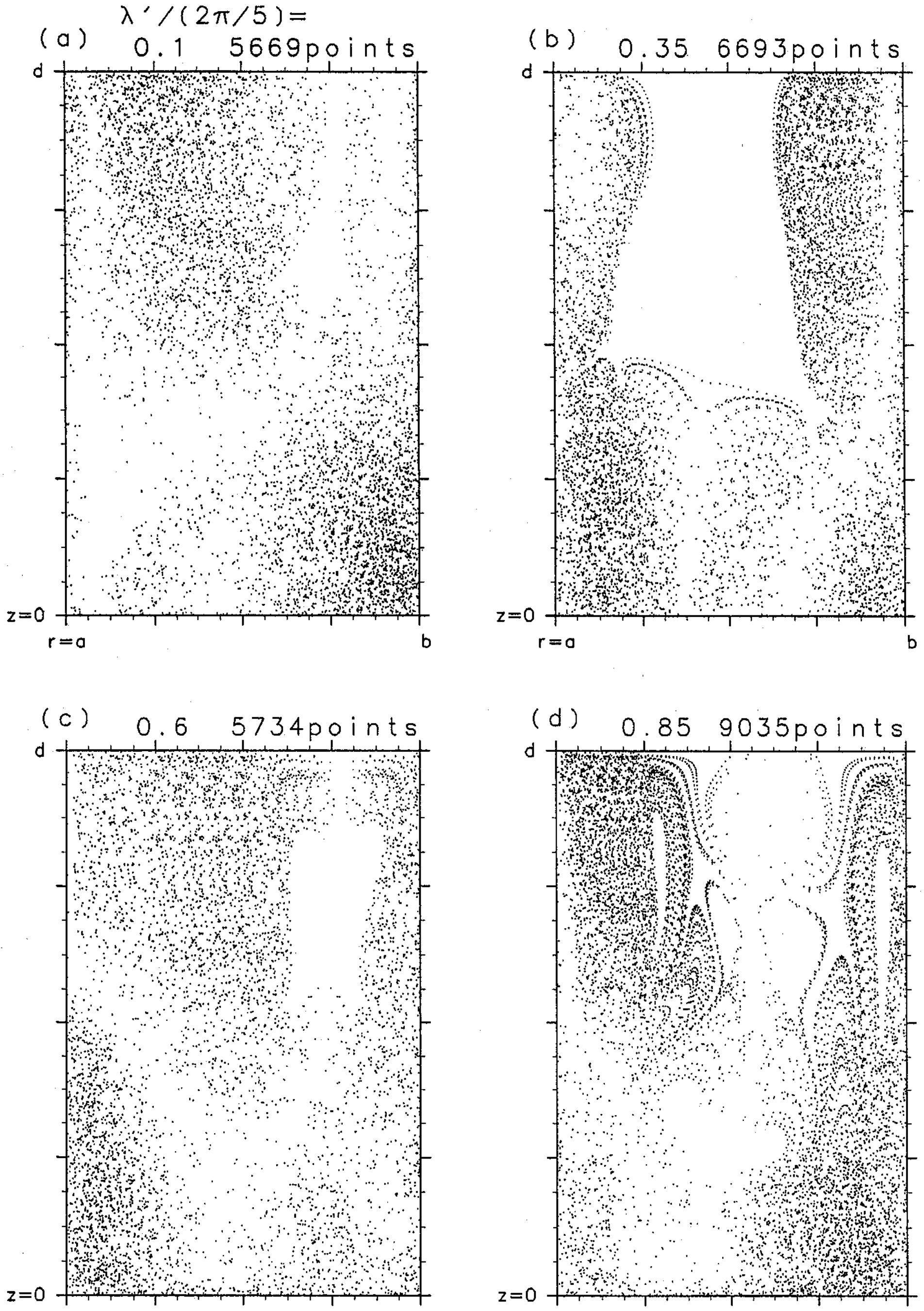

Fig. 7. As in Fig. 6, except for four meridional sections: $\lambda' = \frac{1}{10} \times \frac{2\pi}{5}$ (a), $(\frac{1}{4} + \frac{1}{10}) \times \frac{2\pi}{5}$ (b), $(\frac{1}{2} + \frac{1}{10}) \times \frac{2\pi}{5}$ (c), and $(\frac{3}{4} + \frac{1}{10}) \times \frac{2\pi}{5}$ (d).

Here x and y are "distance" from the grids:

$$r = a + \Delta r(i + x), \tag{5}$$

$$z = \Delta z(j + y), \tag{6}$$

where Δr and Δz are the radial and vertical grid intervals, respectively. Interpolation in the λ direction is not necessary because of the semi-spectral model. Within one grid from a boundary, a modification of the interpolation is necessary for the velocity component normal to the boundary in order to prevent the particle from penetrating the boundary. For example, the radial velocity within one grid distance from the inner wall, $u(r, \lambda, z)$ is given by

$$u(r, \lambda, z) = x^2(1 - y)u_{1,j} + x^2 y u_{1,j+1}, \tag{7}$$

which approximation satisfies the mass conservation law. Similar modification is done for the other three boundaries.

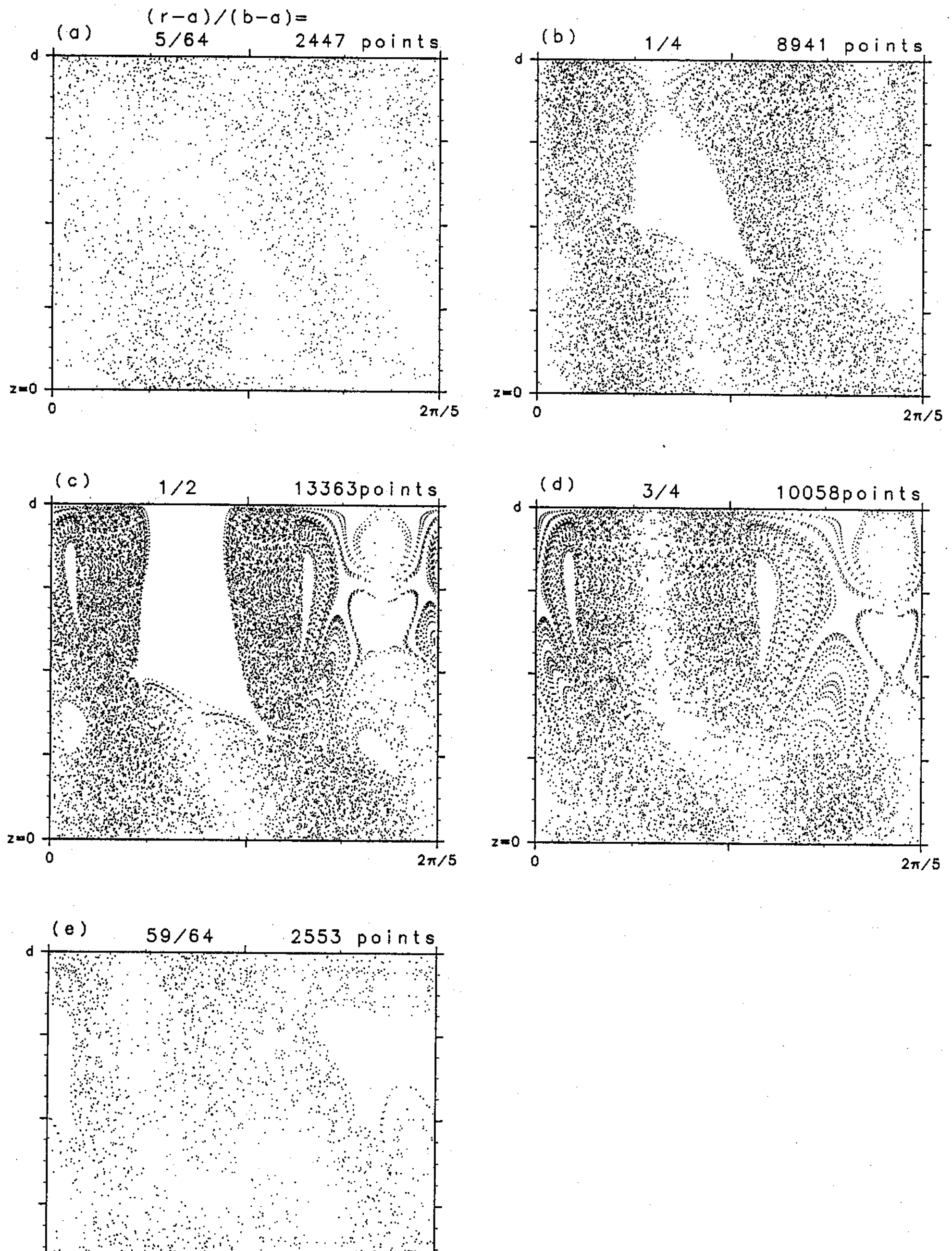

Fig. 8. As in Fig. 6, except for five azimuthal sections: $(r-a)/(b-a) = 5/64$ (a), 1/4 (b), 1/2 (c), 3/4 (d), and 59/64 (e).

2.3 Trajectory of a particle motion

Trajectory of a particle motion is projected onto the r-λ' plane, r-z plane, and λ'-z plane in Fig. 5. Even for the present steady-wave solution, the trajectory in the co-moving frame is highly complicated and shows a chaotic nature. However, the particle motion is not random but has some coherent structures. For example, two predominant wavy streaks appear in the horizontal projection (a), of which crests are nearly out of phase in the azimuthal direction. The interior region of the meridional projection (b) is occupied by nearly horizontal streak lines which slope up toward the inner wall, while side boundary layers are occupied by vertical streak lines. The azimuthal projection (c) mostly consists of horizontal streak lines in consistency with the meridional projection.

A method of Poincaré sections in the study of dynamical systems is used for detailed visualization of the Lagrangian structure of the steady annulus wave as Dombre *et al.* (1986) used the method for the ABC flows. Only the successive intersections of trajectories with one or several surfaces, which are called Poincaré sections, are plotted to get a two-dimensional picture of the three-dimensional trajectories. Figure 6 shows four horizontal Poincaré sections at $z/d = 3/4$ (a), $1/2$ (b), $1/4$ (c), and $1/16$ (d). The last section (d) is nearly at the top of the lower boundary layer (the Ekman layer). The points of intersections are scattered on the horizontal planes except for some empty regions, the largest one of which is in the low-pressure at upper- and mid-levels (a, b). The points in the side boundary layers are clearly separated from those in the interior with a sparse band because the vertical velocity is nearly zero around the interface to form the sparse band. The points are also sparse along the line of $w = 0$ (Fig. 4b) in the interior. A cluster of the points in the low-pressure at the top of the lower boundary layer (d) is suggestive of frequent upward passage of the particle due to the Ekman pumping. Any "ordered" region of the points is not obtained in the horizontal sections, which is an reflection of the fact that trajectories in the interior are quasi-horizontal.

If vertical sections are used for the Poincaré plot, some ordered regions are obtained as well as other chaotic regions. Figure 7 shows four meridional Poincaré sections at $\lambda' = (n/4 + 1/10) \times 2\pi/5, (n = 0, 1, 2, 3)$, which nearly correspond to the trough (b), the ridge (d), and the middle between them (a, c) in the upper layers. An ordered region exists around the high-pressure in the upper and middle layers (d), in which successive points of intersections lie on a well-defined curve. Another vertical section along $r = (a+b)/2$ (Fig. 8c) shows topologically symmetric structure of the curves with respect to the center of the high-pressure. In three-dimensional space each trajectory lies on a two-dimensional surface of a tube around the high-pressure center. Several empty regions which have a ring structure are found around the high-pressure center.

Another ordered region exists around the low-pressure center in the upper and middle layers, as shown in Figs 7b, 8b and 8c. The ordered region is not so large as that around the high-pressure center. More impressively a large volume of empty region exists within the ordered region around the low-pressure center. The marked particle has never entered the region in over 5×10^5 s. On the other hand, any particle which is initially placed in the empty region does not go outside for the same order of time period but has a quasi-periodic orbit on a torus around the low-pressure. For the quasi-periodic orbit, a couple of closed rings are obtained in vertical Poincaré sections (not shown).

Several clusters of the points in chaotic regions are observed in the meridional and azimuthal Poincaré sections (Figs. 7 and 8). One group of the clusters is related to the westerly jet stream in the upper layers, and another group is related to the jet stream in the lower layers which is easterly in the co-moving frame. These two clusters are easily discernible in Fig. 7a and 7c. Some of the vertical Poincaré sections show clusters of the points related with the side and lower boundary layers.

2.4 Division into seven regions by the particle behavior

Figure 9 shows time variations of the position of the particle in the co-moving frame (r, λ', z), pressure p, and normalized temperature θ for 20,000 s from $t = 20,000$ s to $t = 40,000$ s. Similarity between the variation of z and p is indicative of the dominance of hydrostatic balance in the fluid. Each variation is irregular and chaotic. However, some typical ordered behavior appear intermittently, which is in accordance with the chaotic and ordered regions seen in the Poincaré sections (Figs. 6, 7 and 8).

The annular domain except for the empty regions can be divided into seven regions according to the particle behavior: upper-level jet, lower-level jet, cyclonically trapped region, anticyclonically trapped region, inner boundary layer, outer boundary layer and lower boundary layer.

Figure 10 is a bird's eye view of an example of the trajectory during 25,307 s $\leq t \leq 26,100$ s ((1)–(4) in Fig. 9). The particle is in the lower-level jet from (1) to (2); it is advected westward relative to the wave (*i.e.*, retrograde, $d\lambda'/dt < 0$) with large meandering. The particle rotates nearly two rounds in the annulus and the center of the meander shifts outward. It enters the outer boundary layer (2), moves upward and westward for a while, and enters the upper-level jet (3). The particle in the upper-level jet progrades to the wave with large meandering. It rotates over one round and the center of the meander shifts inward. It finally enters the inner boundary layer (4). Particle motion in the upper-level jet and in the lower-level jet is distinguishable by the rapid prograde and retrograde, respectively, in the λ' section in Fig. 9.

Another example of the trajectory in the anticyclonically trapped region and in the cyclonically trapped region is shown in Fig. 11 for the duration of 29,148 s $\leq t \leq 31,931$ s corresponding to (a)–(d) in Fig. 9. The particle spirals up from (a) to (b) and down from (b) to (c) in the anticyclonically trapped region. The downward spiral is inside of the upward spiral. The particle enters the cyclonically trapped region (c), spirals up in the region, and finally enters the inner boundary layer (d). These trajectories in the trapped regions make the ordered regions in the Poincaré sections (Figs. 7 and 8). Par-

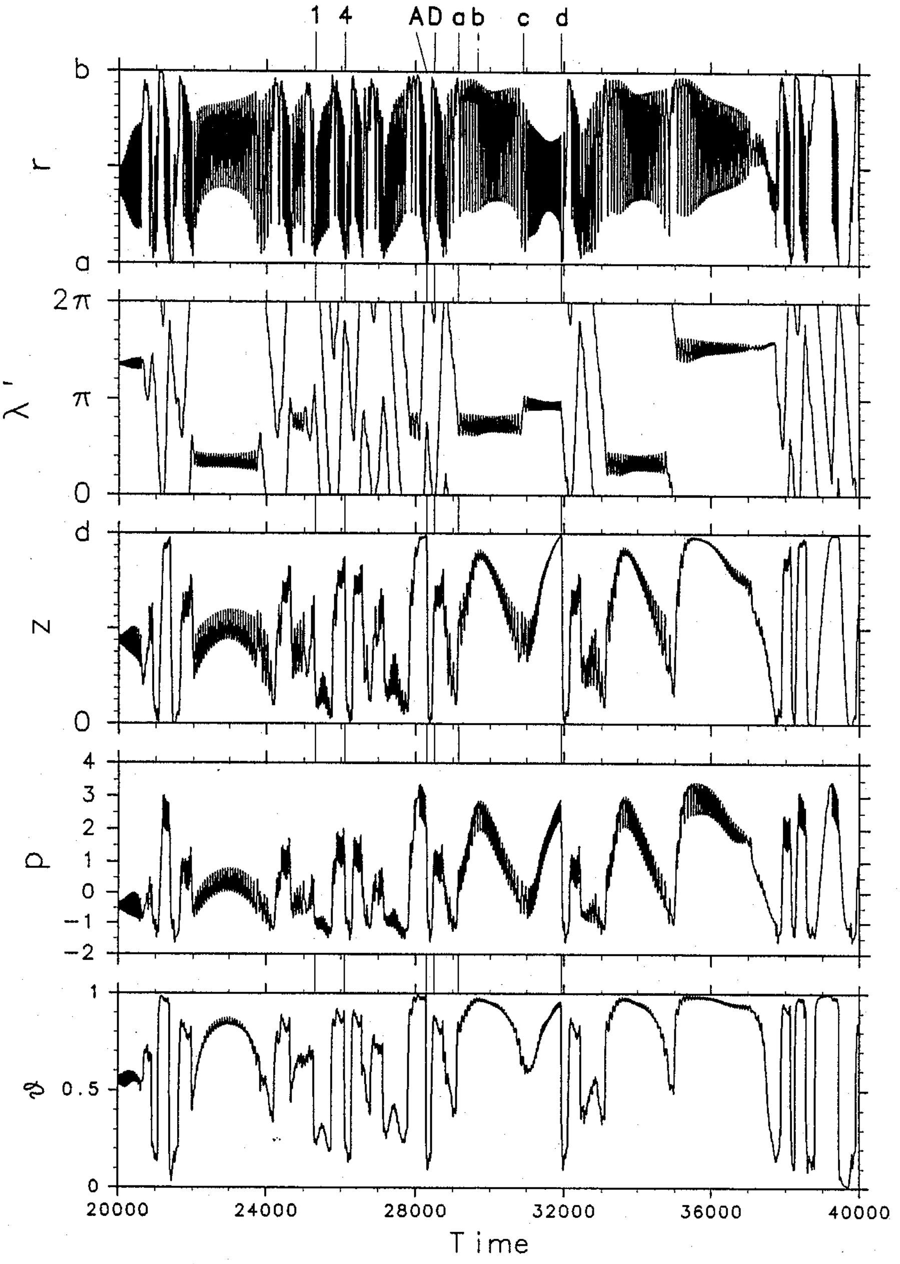

Fig. 9. Time variations of each variable following the marked particle: (a) radius r [cm], (b) azimuth λ' [rad], (c) height z [cm], (d) pressure divided by mean density p [$\mathrm{cm}^2/\mathrm{s}^2$], and (e) normalized temperature θ. The period is 2×10^4 s from $t = 2 \times 10^4$ s to 4×10^4 s.

ticle motion in these trapped regions is easily distinguished by the oscillation of λ' around a particular phase in Fig. 9; other durations in the anticyclonically trapped region are 21,993 s $\leq t \leq$ 23,975 s, 33,137 s $\leq t \leq 34,849$ s, 35,049 s $\leq t \leq 37,743$ s, and so on, and those in the cyclonically trapped region are 20,000 s $\leq t \leq 20,724$ s and so on.

Figure 12 is the third example of the trajectory showing a typical particle motion in three boundary layers for the duration of 28,286 s $\leq t \leq 28,492$ s corresponding to (A)–(D) in Fig. 9. The particle moves downward and westward relative to the wave from (A) to (B) in the inner boundary layer and enters the lower boundary layer. The particle moves outward with some meandering to enter the outer boundary layer, in which it moves upward and westward rapidly. Particle motion in the inner (outer) boundary layer is distinguished in Fig. 9 by the closeness of r to $a(b)$ and rapid decrease (increase) of z, while that in the lower boundary layer by the closeness of z to 0.

The marked particle stays in one of the above seven regions for some period of time and makes a transition to another region. Residence time in

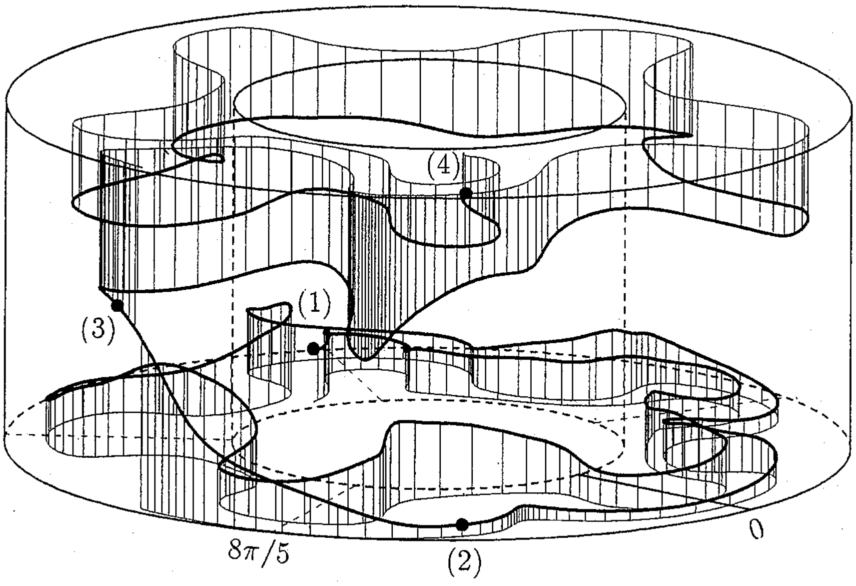

Fig. 10. Bird's-eye view of a trajectory in the lower-level jet and the upper-level jet. Each label corresponds to a particular time; $t = 25,307$ s (1), 25,748 s (2), 25,794 s (3), and 26,100 s (4). Thin vertical lines are projections of the trajectory onto the upper boundary or the lower boundary with an interval of two seconds.

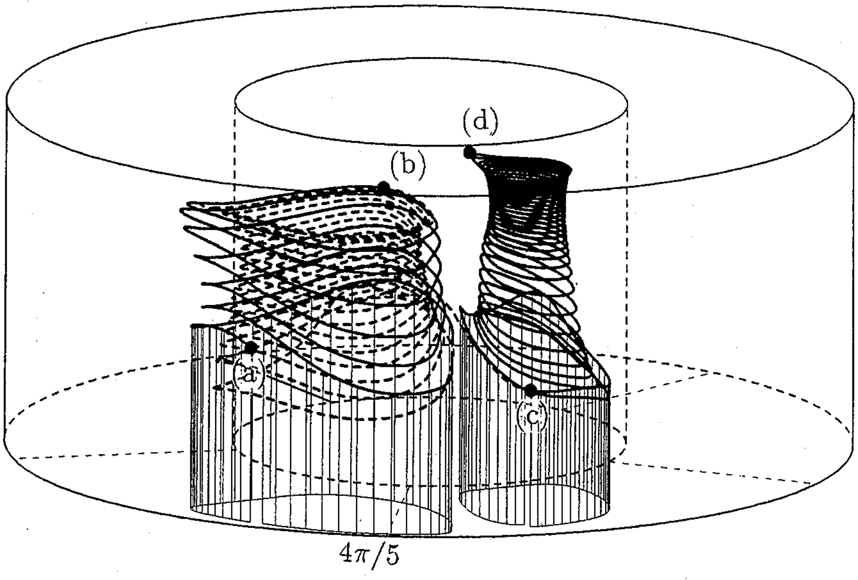

Fig. 11. As in Fig. 10, except for the anticyclonically trapped region and the cyclonically trapped region. Each label corresponds to a particular time; $t = 29,148$ s (a), 29,676 s (b), 30,904 s (c), and 31,931 s (d). The line between (b) and (c) is drawn by a broken line. Vertical projection is done every two seconds.

each region and transitions between the regions are computed with the trajectory of 10^5 s period at the beginning.

The first column of Table 1 is the number of dwell periods (N) of the particle in each region. It stays nearly 100 times in each region of the upper-level jet, the inner boundary layer, and the outer boundary layer. The number N for the lower-level jet is nearly 2/3 of the largest value and those for the lower boundary layer and the anticyclonically trapped region are nearly 1/3. The cyclonically trapped region has the least number ($N = 22$). However, the total time T (the second column of Table 1) and the average time T/N (the last column) of the stay in each region have different orders in length. The particle stays longest in the anticyclonically trapped region

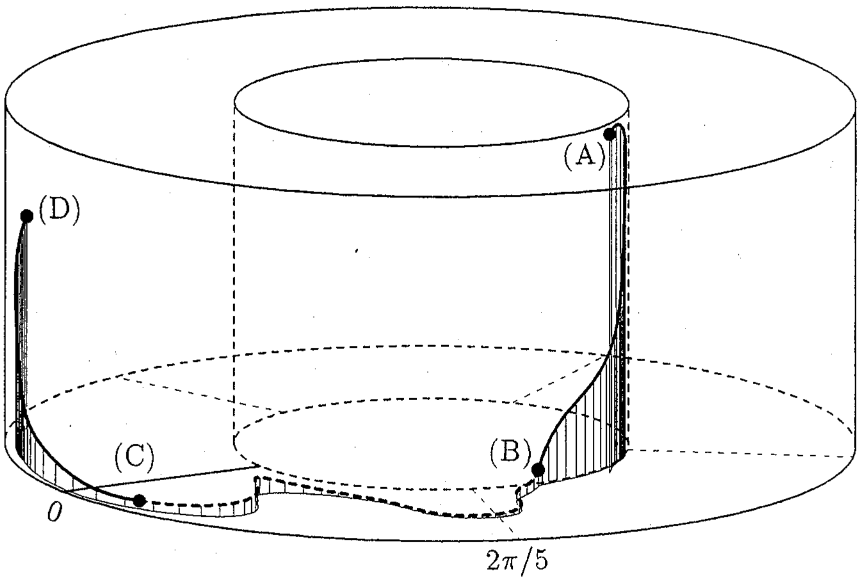

Fig. 12. As in Fig. 10, except for three boundary layers. Each label corresponds to a particular time; $t = 28,286$ s (A), 28,342 s (B), 28,431 s (C), and 28,492 s (D). Vertical projection is done every two seconds.

Table 1. Number of dwell periods (N) of the particle in each region, total time (T) of the stay, and average time (T/N) of the stay.

region	number (N)	total time (T) [s]	average time (T/N) [s]
Upper-level jet	101	21,457	212.4
Lower-level jet	64	19,531	305.2
Cyc. trapped	22	15,732	715.1
Anticyc. trapped	34	26,597	782.2
Inner boundary	96	4,907	51.1
Outer boundary	103	8,971	87.1
Lower boundary	36	2,805	77.9
Sum	456	100,000	219.3

over 1/4 of 10^5 s. The total time of the stay in the upper-level jet, the lower-level jet and the cyclonically trapped region has the same order of 10^4 s as the largest T, while that in the three boundary layers is one order smaller. On average, residence time is longest (over 700 s) in the two trapped regions. Once the particle enters these trapped regions, it spirals with a slow speed, as shown in Fig. 11; the longest residence time is 3,456 s in the cyclonically trapped region. The average residence time in the lower-level jet is less than 1/2 of those in the trapped regions, and that in the upper-level jet is less than 1/3. The average residence time in the boundary layers is one order smaller than that in the four interior regions.

2.5 Transitions between the regions

The number of transitions from one region to another is counted for the total 455 transitions to make a transition matrix (Table 2). Dominant transitions whose number exceeds five are also illustrated in Fig. 13. Transition between regions is not unique but has a probability distribution, that is to say, the region transition is not periodic (cyclic) but chaotic. However, six transitions take place much more frequently than the other transitions, as indicated by boldface in the table and thick arrows in Fig. 13. A very frequent route of the transition exists from the outer boundary layer to the inner boundary layer via the upper-level jet. The route from the inner boundary layer is divided into the lower-level jet and the lower boundary layer, and then confluent to the outer boundary layer; these six preferred transitions constitute a cyclic route with a split of the lower-level jet and the lower boundary layer. An example of the route, the lower-level jet → the outer boundary layer → the upper-level jet → the inner boundary layer, was already shown in Fig. 10 and that of the inner boundary layer → the lower boundary layer → the outer boundary layer in Fig. 12. Sum of the transitions on this route accounts for more than 3/4 of the total transitions.

As for the transitions concerning the cyclonically trapped region, transition from the anticyclonically trapped region as shown in Fig. 11 and that to the outer boundary layer are most preferred. On the other hand, two preferred transitions to the anticyclonically trapped region are from the outer and the inner boundary layers, while three preferred tran-

Table 2. Transition matrix. The number of transition from one region to another is counted for the total of 455 transitions.

		To							
	region	U.J.	L.J.	C.T.	A.T.	I.B.	O.B.	L.B.	Sum
From	Upper-level jet	–	3	5	3	**88**	2	0	101
	Lower-level jet	1	–	4	0	2	**57**	0	64
	Cyc. trapped	2	4	–	4	4	8	0	22
	Anticyc. trapped	9	10	10	–	2	2	0	33
	Inner boundary	0	**47**	1	12	–	0	**36**	96
	Outer boundary	**88**	0	0	15	0	–	0	103
	Lower boundary	0	0	2	0	0	**34**	–	36
	Sum	100	64	22	34	96	103	36	455

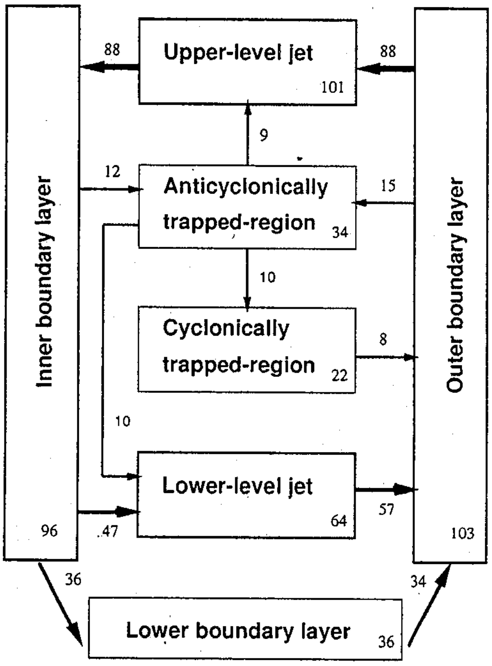

Fig. 13. Frequent routes of the transition between seven regions. Thick, medium and thin arrows are indicative of the frequency.

sitions from the anticyclonically trapped region are to the upper-level jet, the lower-level jet and the cyclonically trapped region. Note that the transitions to these trapped regions are largely different from each other; preferred transitions to the cyclonically trapped region are from the other three interior regions, while those to the anticyclonically trapped regions are from the two side boundary layers.

The inner boundary layer is only the region for entry to the lower boundary layer in this 10^5 s. Most of the transitions from the lower boundary layer are to the outer boundary layer but two of those are the Ekman pumping to the cyclonically trapped region.

Each transition takes place at the interface between two regions in physical space. For example, the interface between the upper-level jet and the inner boundary layer is located in the ridge in the upper layer, as shown by a cluster of the points of intersections in Fig. 8a. The anticyclonically trapped region has an interface with the outer boundary layer in the upper layer and with the inner boundary layer in the lower layer, as shown in Fig. 8a and 8e (vice versa for the cyclonically trapped region), because the upper and the lower jet streams flow opposite direction of λ' in the co-moving frame.

3. Lagrangian view of the heat transport

The total inward heat flux in the present steady wave solution is 14.6 J/s, which is independent of r because of the steadiness. Figure 14 shows the zonally-averaged flux vector in the meridional plane: total heat flux (a) and three components of that due to thermal diffusion (b), mean meridional circulation (c) and deviatoric (wave) flow (d). In this Eulerian description heat enters in the lower part of the outer side boundary by diffusion and is transported inward mainly by the mean meridional circulation. The deviatoric flow plays a dominant role in the middle of the annulus. The mean meridional circulation transports heat near the inner side boundary and the diffusion is important in the upper part of the inner side boundary. Note that the mean meridional circulation transports heat outward in the middle by indirect circulation, and that the diffusion is negligible almost everywhere except for the side boundary layers. The inward heat flux is caused by both inward motion of warm particles and outward motion of cold particles. Particles are warmed up in the outer boundary layer and cooled down in the inner boundary layer. However, details of the temperature variation following the Lagrangian motion of particles is not clear.

Figure 15 shows the time variation of the temperature following the particle and its time derivative (a) along with the radius r and the height z of it (b) during 25,000 s $\leq t \leq 32,000$ s, which period is a

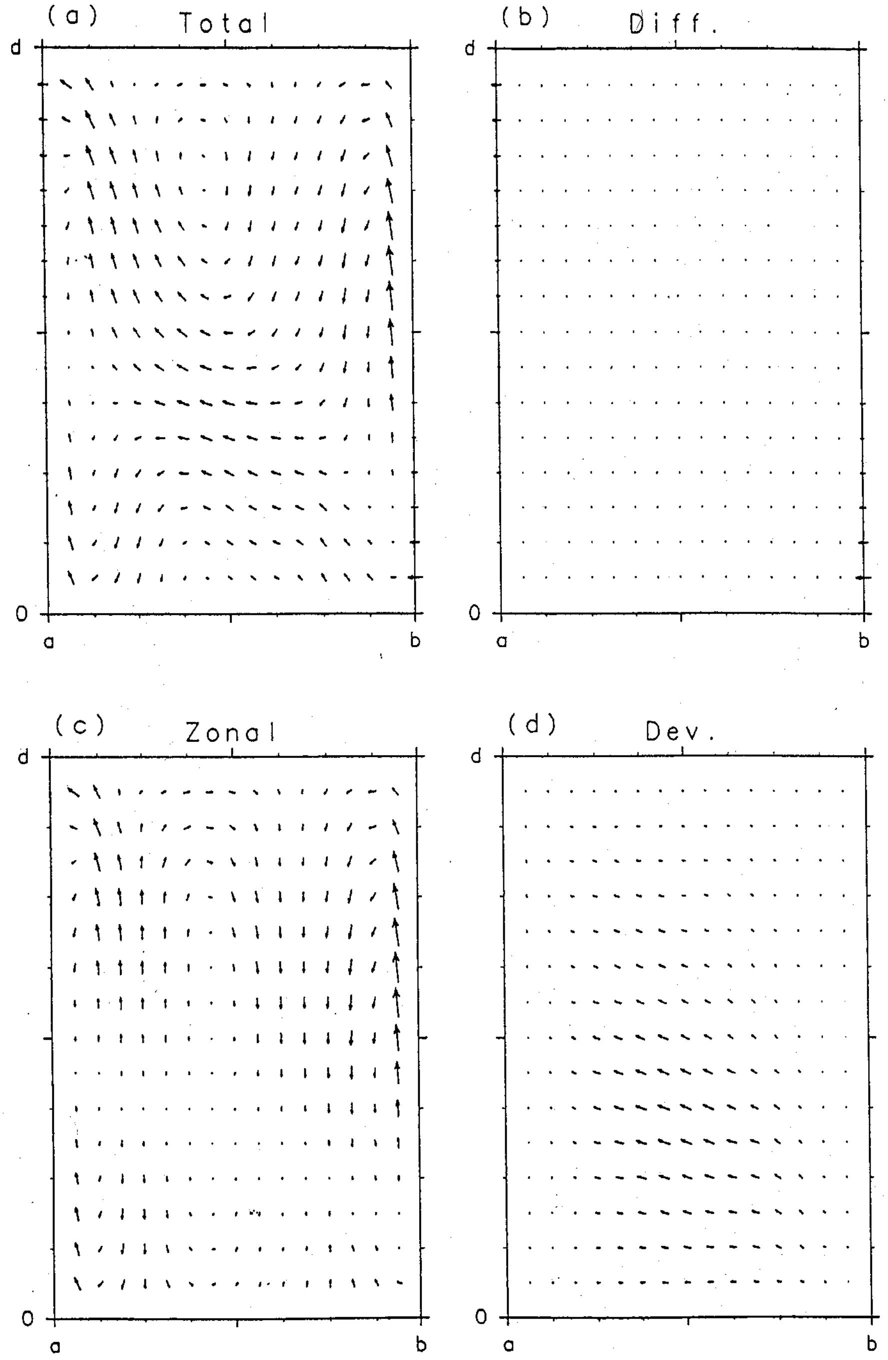

Fig. 14. Meridional distributions of heat flux divided by fluid density and specific heat; (a) total flux, (b) that due to diffusion $(-r\kappa\frac{\partial\bar{\theta}}{\partial r}, -r\kappa\frac{\partial\bar{\theta}}{\partial z})$, (c) that due to mean meridional circulation $(r\bar{u}(\bar{\theta}-0.5), r\bar{w}(\bar{\theta}-0.5))$, and (d) that due to wave $(\overline{ru'\theta'}, \overline{rw'\theta'})$.

part of that shown in Fig. 9. The trajectories shown in Figs. 10, 11 and 12 are within this period. Large changes of temperature occur when the particle is in the two side boundary layers, which fact means that the particle largely gets heat in the outer boundary layer and loses it in the inner boundary layer with the diabatic vertical motions, as shown in Fig. 5b. Temperature change is rather small in the other five regions. The last column of Table 3 shows the net temperature change ($\Delta\Theta$) of the particle during its stay in each region. The absolute values $|\Delta\Theta|$ in the side boundary layers are more than 0.6, which are much larger than those in the other regions.

As for the time variations within the upper-level jet and the lower-level jet, the temperature of the particle does not change very much during its stay,

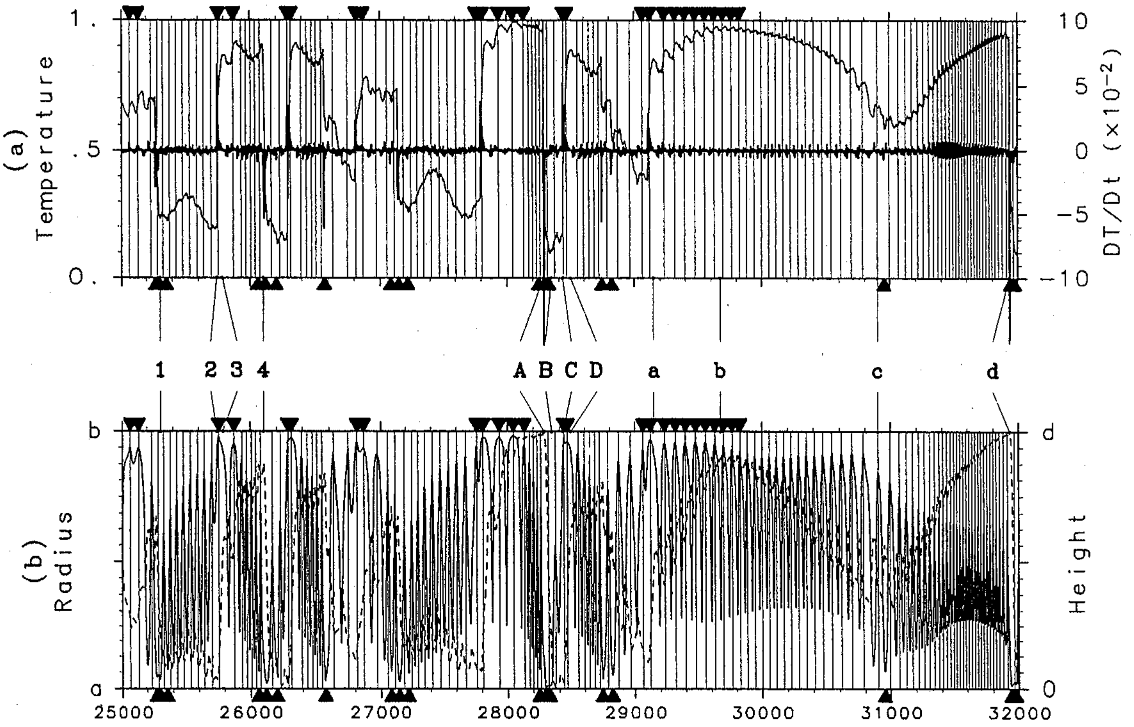

Fig. 15. Time variations of each quantity following the marked particle during 25,000 s $\leq t \leq 32,000$ s: (a) normalized temperature θ (solid line) and time-derivative of the temperature $D\theta/Dt$ (shaded area), and (b) radius r (solid line) and height z (broken line). Thin vertical lines indicate the times when the radius has a local maximum. Triangle marks at the top and bottom of each figure indicate the time when the particle approaches the outer and inner boundary most closely, respectively, within the side boundary layers. Labels **1**–**4**, **A**–**D**, and **a**–**d** correspond to the labels in Figs.10, 11 and 12, respectively.

Table 3. Temperature increase (Θ_+) and decrease (Θ_-) of the particle during any stay in each region and the net change ($\Delta\Theta \equiv \Theta_+ - \Theta_-$), which are averaged values for the 10^5 s period.

region	temperature increase (Θ_+)	temperature decrease (Θ_-)	Net temperature change ($\Delta\Theta$)
U.J.	0.00	0.04	−0.04
L.J.	0.02	0.04	−0.01
C.T.	0.15	0.03	0.12
A.T.	0.04	0.09	−0.04
I.B.	0	0.65	−0.65
O.B.	0.62	0	0.62
L.B.	0.08	0	0.08

nor it does not show clear correlation between heating (cooling) of the particle and its closeness to the outer (inner) boundary during the meanderings of the jet (Fig. 15). Conservation of temperature following the particle motion is roughly fulfilled in the jet regions, because the source and sink term, namely the thermal diffusion term is significant only in the side boundary layers. This Lagrangian view of the heat transport in the steady annulus wave is largely different from the illustration for the atmospheric Rossby circulation, as shown in Fig. 3.

The inward heat flux in the steady annulus wave solution can be estimated crudely from the quantities obtained by the Lagrangian description: the number of region transitions (Table 2) and the temperature change during one stay in each region (Table 3). Suppose that a unit volume of the fluid transports heat $\rho C \Delta T \Delta\Theta$ every S seconds on average, where ρ is the fluid density and C is the specific heat of the fluid, then the total inward heat flux $\mathcal{F}$ is given by

$$\mathcal{F} = \frac{\rho C \Delta T \Delta\Theta}{S} \cdot \pi(b^2 - a^2)d, \qquad (8)$$

if the isolated regions are neglected. Since the particle makes transitions of the cyclic route shown in Fig. 13 nearly 90 times during 10^5 s and its gain of heat in the outer boundary layer and loss in the inner boundary layer are about 0.6 from Table 3, then Eq. (8) gives

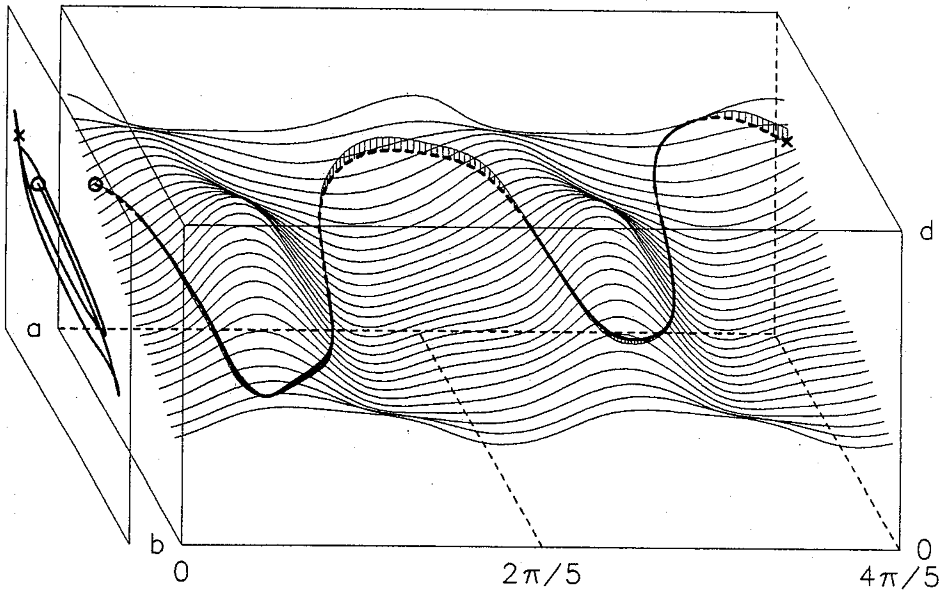

Fig. 16. Bird's-eye view of the trajectory (thick line) of a particle in the upper-level jet during 26,932 s $\le t \le 27{,}088$ s. Thin curved lines indicate an isothermal surface of $\theta = 0.72$. The trajectory is drawn by a solid line when the particle is above the surface and by a broken line when it is below the surface. Vertical lines are projections of the trajectory onto the isothermal surface every second.

$$\begin{aligned}\mathcal{F} &= \frac{0.997\ \mathrm{g/cm^3} \times 4.18\ \mathrm{J/(g\cdot K)} \times 3\ K \times 0.6}{10^5\ \mathrm{s}/90} \\ &\quad \times \pi\{(9.7\ \mathrm{cm})^2 - (4.5\ \mathrm{cm})^2\} \times 8\ \mathrm{cm} \\ &= 12.5\ \mathrm{J/s}, \qquad (9)\end{aligned}$$

which is roughly comparable to that obtained by the exact Eulerian calculation (14.6 J/s). This correspondence is indicative of the appropriateness of the present Lagrangian description.

4. Discussion

Some isolated regions around the low-pressure and high-pressure centers were found in the analysis of particle trajectories, which were shown as empty regions in the Poincaré sections of Figs. 6, 7 and 8. Exchange of the particle between the isolated regions and others does not take place, even over a long period. Existence of these isolated regions is basically explained by the two-dimensional trapping mechanism within the propagating disturbances (Flierl, 1981), because the trajectories are quasi-horizontal. However, different structures between the isolated regions around the low-pressure and the high-pressure centers come from the three-dimensionality of the flow field; difference in a weak but non-zero vertical velocity field produces the structural difference between the two isolated regions.

A projection of trajectories on the meridional plane (Fig. 5b) shows similar behavior of particles as in the laboratory experiment (Fig. 2); nearly elliptic orbits with a tilt of the major axis from upper inside to lower outside. An example of a particle trajectory in the upper-level jet is shown in Fig. 16 with a three-dimensional view of an isothermal surface. As suggested by Sakai (1990), the particle moves nearly on the surface because of the nearly adiabatic motion in the interior; it moves inward along the "trough" of the isothermal surface and outward along the "ridge" of the surface. As a result, the projection of the trajectory shows an elliptic "indirect circulation". The large meander of the trajectory on the surface is determined mainly by the horizontal velocity field as shown in Fig. 4e or, more precisely, by the conservation of the Ertel's potential vorticity following the motion.

To get a gross feature of the chaotic Lagrangian motion a new approach was introduced by computing the residence time in each region, into which the annulus of fluid was divided based on the particle behavior, and by making a transition matrix between the regions. A remarkably preferred cyclic-route of transitions was obtained in the analysis and inward heat transport was reinterpreted based on the Lagrangian data. In the preferred route a particle gets large amount of heat in the outer boundary layer and enters the upper-level jet. It moves nearly adiabatically in the interior, enters the inner boundary layer, and releases the heat. It returns to the outer boundary layer via the lower-level jet or the lower boundary layer. This picture is consistent with the "direct one-cell circulation" based on the Lagrangian description (see *e.g.*, Kida, 1977, 1983), even though the Lagrangian motion has indirect circulation *within* the jet regions as shown in Figs. 2 and 16. In the jet regions, particles move nearly adiabatically in contrast with the illustration in Fig. 3 for the general circulation of the atmosphere.

In this study particle trajectories were computed for a very long period. The obtained trajectory is sensitive to the initial condition, the time integration scheme, or the time interval for the integration because of the chaotic nature of the trajectory in the present solution. However, the general structure of the ordered and chaotic regions and the gross feature of the regime transitions are not very sensitive to those mentioned above. For example, if another initial condition is adopted for the tracer particle, elements of the transition matrix are not identical to those listed in Table 2 but the gross feature of the regime transitions is not very different from that summarized in Fig. 13.

We considered an idealized particle of which motion is governed by the deterministic equation (2). Most of the studies on "chaotic advection" or "Lagrangian turbulence" have been done under this assumption. A possible realization of the particle in laboratory experiments is the small tracer particles used by Solomon *et al.* (1993), which are small enough (approximately 1mm in size) to ensure that they follow the flow faithfully. However, Eq. (2) may not be very appropriate when we investigate the diffusion of dye locally injected in laboratory experiments, an example of which is that on vortices and Rossby waves in eastward and westward jets by Sommeria *et al.* (1988, 1989, 1991). It is neccesary to consider the random processes due to molecular motions explicitly by introducing a stochastic forcing term. Such a stochastic forcing has been used in long-range atmospheric transport models for the effect of "eddy diffusion" (*e.g.*, Takasugi and Nakamura, 1988; Sullivan *et al.*, 1993).

5. Conclusions

Lagrangian motion of a tracer particle was numerically investigated for a steady wave solution in a rotating annulus fluid. Trajectory of the particle was traced for a long period of 5×10^5 s in the co-moving frame with the steady wave. The trajectory shows a chaotic nature (Fig. 5) even though the Eulerian flow field is regular (Fig. 4). The three-dimensional structure of the chaotic trajectory was obtained with several Poincaré sections (Figs. 6–8), which show some typical organized behavior, depending on the particle position in the annulus. The annulus of fluid can be divided into the following regions based on the particle behavior: the upper-level jet, the lower-level jet, the cyclonically trapped region, the anticyclonically trapped region, the inner boundary layer, the outer boundary layer, and the lower boundary layer. A large isolated region in which the marked particle had never stayed was also found inside the cyclonically trapped region, and some other isolated regions were found around the anticyclonically trapped region. The upper-level jet is an untrapped region, where the particle moves eastward with large meander and drifts inward gradually every meander. The lower-level jet is another untrapped region, where the particle moves westward relative to the wave and drifts outward. On the other hand, in the cyclonically trapped region and anticyclonically trapped region, the particle spirals up and down around the center of low-pressure and that of high-pressure, respectively. Vertical Poincaré sections clearly show that these trapped regions are "ordered" regions of the points of intersections in contrast to other "chaotic" regions. Any particle which is initially placed in the isolated regions has a quasi-periodic orbit on a torus.

The number of dwell periods and the average time of the stay of the particle in each region were computed with the trajectory data of the initial 10^5 s period (Table 1), and the number of transitions from one region to another was counted for the total of 455 transitions (Table 2). Transition between the regions has a probability distribution (namely, the transition matrix) because of the chaotic nature of the trajectory. However, a cyclic route of the transitions, which partly branches out into two, was found to be remarkably preferred: the outer boundary layer → the upper-level jet → the inner boundary layer → the lower-level jet or the lower boundary layer → the outer boundary layer.

The temperature change of the same particle was computed for a long time period. The particle absorbs a large amount of heat in the outer boundary layer through diabatic upward motion and releases a large quantity of heat in the inner boundary layer through diabatic downward motion. Temperature is nearly conserved following the particle motion in the other regions (Table 3). Since there is not a significant correlation between the temperature change and radial movement in either of the jet regions, little heat is transported in any one cycle of the meander of the jets. A crude estimation of the inward heat flux using the frequency of the transitions between the side boundary layers and temperature change in the layers gives a value comparable to the exact Eulerian calculation, which fact is indicative of the appropriateness of the present Lagrangian description.

Acknowledgments

We wish to thank Professor I. Hirota for his valuable comments and encouragement. We also wish to thank Dr. S. Sakai for providing us with the experimental data, and Drs. A. Numaguti, M. Satoh, and M. Yamada for their valuable comments. The GFD-DENNOU Library was used for drawing the figures.

References

Bajer, K. and H.K. Moffatt, 1990: On a class of steady confined Stokes flows with chaotic streamlines. *J. Fluid Mech.*, **212**, 337–363.

Behringer, R.P., S.D. Meyers and H.L. Swinney, 1991: Chaos and mixing in a geostrophic flow. *Phys. Fluids A*, **3**, 1243–1249.

Dombre, T., U. Frisch, J.M. Greene, M. Hénon, A. Mehr and A.M. Soward, 1986: Chaotic streamlines in the ABC flows. *J. Fluid Mech.*, **167**, 353–391.

Flierl, G.R., 1981: Particle motions in large-amplitude wave fields. *Geophys. Astrophys. Fluid Dyn.*, **18**, 39–74.

Hide, R. and P.J. Mason, 1975: Sloping convection in a rotating fluid. *J. Adv. Phys.*, **24**, 47–100.

Kida, H., 1977: A numerical investigation of the atmospheric general circulation and stratospheric-tropospheric mass exchange: II. Lagrangian motion of the atmosphere. *J. Meteor. Soc. Japan*, **55**, 71–88.

Kida, H., 1983: General circulation of air parcels and transport characteristics derived from a hemispheric GCM Part 2. Very long-term motions of air parcels in the troposphere and stratosphere. *J. Meteor. Soc. Japan*, **61**, 510–523.

Knobloch, E. and J.B. Weiss, 1987: Chaotic advection by modulated traveling waves. *Phys. Rev. A*, **36**, 1522–1524.

Ottino, J., 1989: *The kinematics of mixing: stretching, chaos and transport.* Cambridge University Press, p. 264.

Pierrehumbert, R.T., 1991a: Large-scale horizontal mixing in planetary atmospheres. *Phys. Fluids A*, **3**, 1250–1260.

Pierrehumbert, R.T., 1991b: Chaotic mixing of tracer and vorticity by modulated travelling Rossby waves. *Geophys. Astrophys. Fluid Dyn.*, **58**, 285–319.

Pierrehumbert, R.T. and H. Yang, 1993: Global chaotic mixing on isentropic surfaces. *J. Atmos. Sci.*, **50**, 2462–2480.

Rossby, C.G. and Collaborators, 1937: Aerological evidence of large-scale mixing in the atmosphere. *Trans. Am. Geophys. Union*, **18**, 130–136.

Sakai, S., 1990: (personal communication).

Solomon, T.H., E.R. Weeks and H.L. Swinney, 1993: Observation of anomalous diffusion and Lévy flights in a two-dimensional rotating flow. *Phys. Rev. Letter*, **71**, 3975–3978.

Sommeria, J., S.D. Meyers and H.L. Swinney, 1988: Laboratory simulation of Jupiter's Great Red Spot. *Nature*, **331**, 689–693.

Sommeria, J., S.D. Meyers and H.L. Swinney, 1989: Laboratory model of a planetary eastward jet. *Nature*, **337**, 58–61.

Sommeria, J., S.D. Meyers and H.L. Swinney, 1991: Experiments on vortices and Rossby waves in eastward and westward jets. *Nonlinear Topics in Ocean Physics, A., R., Osborne. Ed., North-Holland*, **337**, 227–269.

Sugata, S. and S. Yoden, 1993: A numerical study on régime transitions of the rotating annulus flow with a semi-spectral model. *J. Meteor. Soc. Japan*, **71**, 491–501.

Sullivan, T.J., J.S. Ellis, C.S. Foster, K.T. Foster, R.L. Baskett, J.S. Nasstrom and W.W. Schalk III, 1993: Atmospheric release advisory capability: Real-time modeling of airborne hazardous materials. *Bull. Amer. Meteor. Soc.*, **74**, 2343–2361.

Takasugi, T. and H. Nakamura, 1988: A tracer diffusion model coupled with the JMA global spectral model. JMA/NPD Tech. Report. No. 24, p. 49.

Ukaji, K. and K. Tamaki, 1989: A comparison of laboratory experiments and numerical simulations of steady baroclinic waves produced in a differentially heated rotating fluid annulus. *J. Meteor. Soc. Japan*, **67**, 359–374.

Unno, W., S. Ueda and M. Komabayashi, 1992: "CHIGAKU" ("Earth Science" in Japanese). Tokyoshoseki Co. Inc., p. 312.

Weiss J.B. and E. Knobloch, 1989: Mass transport and mixing by modulated traveling waves. *Phys. Rev. A*, **40**, 2579–2589.

Welander, P., 1955: Studies on the general development of motion in a two-dimensional, ideal fluid. *Tellus*, **7**, 141–156.

Williams, G.P., 1969: Numerical integration of the three-dimensional Navier-Stokes equations for incompressible flow. *J. Fluid Mech.*, **37**, 727–750.

Williams, G.P., 1971: Baroclinic annulus waves. *J. Fluid Mech.*, **49**, 417–449.

Williams, G.P., 1972: The field distributions and balances in a baroclinic annulus wave. *Mon. Wea. Rev.*, **100**, 29–41.

Yoden, S. and M. Nomura, 1993: Finite-time Lyapunov stability analysis and its application to atmospheric predictability. *J. Atmos. Sci.*, **50**, 1531–1543.

回転水槽中の定常傾圧波動におけるカオス的ラグランジュ運動と熱輸送

菅田誠治
(国立環境研究所)
余田成男
(京都大学理学部)

回転水槽中の定常傾圧波動におけるラグランジュ運動を、トレーサー粒子の軌跡を数値的に長時間追跡することにより調べた。定常波動の規則的な流れ場においても、軌跡はカオス的な性質を示す。これは「ラグランジュ的乱流」の一例である。しかし、カオス的な軌跡も、その位置に応じて幾つかの組織化された構造を示す。この構造により、粒子の通過した領域は、上・下層ジェット、高・低気圧性トラップ領域、そして内・外・下側の境界層の７つに分けられる。また、粒子が一度も入り込まない孤立領域が、低気圧性トラップ領域の内側や高気圧性トラップ領域を取り巻く位置に存在する。粒子の領域間遷移の長時間にわたる統計により、外側境界層→上層ジェット→内側境界層→下層ジェットまたは下側境界層→外側境界層、の周期的ルートが頻出することが分かった。この周期的ルートと比べて、両トラップ領域に滞在する頻度はかなり少ないが、その滞在時間は長い。

定常波動中の熱輸送をラグランジュ的に見ると、外側境界層で粒子は大量の熱を獲得し、内側境界層でそれを放出している。内部領域では粒子の温度はほとんど変化せず、ジェットの蛇行一回毎の内向き熱輸送は小さい。